The drag force distribution within regular arrays of cubes and its relation to cross ventilation – Theoretical and experimental analyses

(Article begins on next page)

The drag force distribution within regular arrays of cubes and its relation to cross ventilation – theoretical and experimental analyses

Riccardo Buccolieri[a, b*], Mats Sandberg[b], Hans Wigö[b], Silvana Di Sabatino[c]

[a]Dipartimento di Scienze e Tecnologie Biologiche ed Ambientali, University of Salento, S.P. 6 Lecce-Monteroni, 73100 Lecce, Italy

[b]Faculty of Engineering and Sustainable Development, University of Gävle, SE-80176 Gävle, Sweden

[c]Department of Physics and Astronomy, ALMA MATER STUDIORUM - University of Bologna, Viale Berti Pichat 6/2, 40127 Bologna, Italy

Corresponding author: Riccardo Buccolieri

Email: riccardo.buccolieri@unisalento.it

Tel. +39 0832 297 062; fax +39 0832 297 061

Abstract

A novel set of wind tunnel measurements of the drag force and its spatial distribution along aligned arrays of cubes of height H and planar area index λ_p (air gap between cubes) equal to 0.028 ($5H$) to 0.69 ($0.2H$) is presented and analysed. Two different types of measurements are compared: one type where the drag force is obtained using the standard load cell method, another type where the drag force is estimated by measuring the pressure difference between windward and the leeward façades. Results show that the drag force is nearly uniformly distributed for lower λ_p (0.028 and 0.0625), it decreases up to 50% at the second row for λ_p=0.11, and it sharply decreases for larger λ_p (from 0.25 to 0.69) where the force mostly acts on the first row. It follows that for the lowest λ_p the drag force typically formulated as a drag area corresponds to the total frontal area of the array, whereas for large λ_p the drag area corresponds to the area of the first row. By assessing the driving pressure for ventilation from the drag force, the analysis is extended to estimate the cross ventilation as an example of application of this type of measurements.

1. Introduction

Several studies of the modification of the flow due to an array of obstacles exposed to a boundary layer flow have been carried out in the past. These studies can be broadly subdivided into two main categories. One category is based on the classical fluid mechanical approach where the focus is on the evolution of the approaching velocity profile when passing through the array. Usually the array is long enough that an equilibrium is established. An excellent recent example of this approach is given by Thomas et al. (2017), where references to similar studies are provided.

The other category is where the main concern is the ventilation of the array taking into account individual buildings. In this case the focus is on understanding how both the whole array interacts with the approaching wind and how the individual buildings interact with the airflow through the array. The overarching goal of this paper is to contribute to this understanding. This paper is essentially a continuation of our previous work (Buccolieri et al., 2017), where the total drag force was measured in a wind tunnel by using a standard load cell. The focus was to study the effect on the drag force of different building packing density of an array consisting of buildings (represented by cubes) of equal size and shape. A novel method for assessing the distribution of the drag force was introduced by formulating the total drag force as a drag area and then matching this area with the physical façade area of the buildings. One scope here is to validate this method by directly measuring the distribution of the drag force within the array using the same standard load cell method. To provide insight into the quality of the measurements and confidence for the obtained results, the drag force is also assessed by an independent method based on measurements of the surface pressure at the windward and leeward façades of the buildings.

The results are analysed from the perspective that the introduction of an array in a given turbulent flow is a perturbation of a reference case which we have chosen to be the isolated cube. The introduction of new buildings to the reference case increases the resistance (drag) and less air (less flow rate) penetrates into the array compared to the reference case. Therefore it takes a longer time for the approaching air to pass through

the array. This delay has been quantified by Antoniou et al. (2017) for a region within Nicosia in Cyprus by predicting the mean age of air in the city. The delay has a consequence for air quality because the local mean age of air is directly proportional to the concentration in case of homogeneous emissions, see Eq.10 in Buccolieri et al. (2010). Low flow rate penetrating into the array means that less flow available for ventilation of the buildings.

The argument above helps clarifying that the drag is an important parameter linked to both air quality within the array and ventilation potential available for buildings in a given neighbourhood or city. There are several wind tunnel studies reporting on pressure distribution measurements at building façades as well as estimate of the drag force either pressure-derived or using a balance. Cheng and Castro (2002) and Cheng et al. (2007) estimated the drag force on individual cubes within an array by calculating the integral of the pressure difference between the front and the back façades of the cube. Other studies, relevant to the field of wind load on structures, utilized pressure measurements to evaluate the pressure distribution on individual buildings (Kim et al., 2012; Tecle et al., 2013). Zaki et al. (2011) employed surface pressure measurements of the form drag on building arrays featured by both vertical and horizontal randomness as well as different packing densities demonstrating a significant effect of building height variation on aerodynamic parameters when the planar area index is larger than 17%. Li et al. (2015) confirmed the dependence of building shape and position within the array on the drag coefficient by surface pressure measurements. A comprehensive dataset of wind pressure for isolated low- and high-rise buildings, as well as for non-isolated low-rise buildings, is available from the Tokyo Polytechnic University (wind.arch.t-kougei.ac.jp/system/eng/contents/code/tpu).

Cheng et al. (2007), Hagishima et al. (2009) and Zaki et al. (2011) directly measured the drag force using a balance. Cheng et al. (2007) showed that the drag force exerted on cube arrays and derived from measured Reynolds stresses can be underestimated by as much as 25% compared to drag directly measured using a balance. Hagishima et al. (2009) measured the drag force directly by a designed floating raft in a wind tunnel to investigate the aerodynamic effects of various building arrays showing that both wind direction and the height non-uniformity of buildings affect aerodynamic parameters significantly.

96   More recently, few studies have reported measurements of the drag force distribution

97   within building arrays, as done in this paper. Chen et al. (2017) used a standard load cell

98   within arrays consisting of buildings with both the same height and different heights.

99   From the recorded drag force the vertical transport by both advection and turbulence

100   expressed as an exchange velocity was predicted based on methods presented in

101   Bentham and Britter (2003) and in Hamlyn and Britter (2005). Li et al. (2018) reported

102   wind tunnel measurements of the drag distribution within irregular arrays consisting of

103   buildings of different shapes but with the same height. The drag force was estimated

104   from the pressure difference between the windward and leeward façades of the

105   buildings and directly by using floating rafts. They presented drag force distributions

106   and an extensive discussion of estimation of measurements errors and how to conduct

107   this type of measurements is presented.

108   In this context, the novelties of the present paper are briefly summarised:

109   - a comprehensive dataset of recorded drag force including both the total drag force of

110   the whole array (shown in Buccolieri et al., 2017) and the distribution of the drag force

111   within the array for a large span of building packing densities has been created. The

112   dataset includes also data obtained from pressure measurements at the wind- and

113   leeward façades of the buildings;

114   - original analyses are presented showing that an interference between buildings exists

115   and this needs to be quantified in the derivation of the drag force by introducing the

116   wall to wall distance as interference parameter in addition to building area density;

117   - a further validation of the novel method presented in Buccolieri et al. (2017) for

118   assessing the drag force distribution starting from the drag force measurements of the

119   whole array is provided;

120   - an application of the potential usefulness of the dataset is provided by estimating the

121   potential for wind-driven cross ventilation. It is shown that measuring the drag force is

122   much simpler than measuring the pressure in several points.

123

124   **2. Description of wind tunnel experiments**

125   *2.1. The physical models*

126   Measurements were carried out in a closed-circuit boundary layer wind tunnel with a

127   working section 11m long, 3m wide and 1.5m high at the University of Gävle (Sweden)

128   (Fig. 1a). An isolated cube and seven aligned arrays of cubes of planar area index (ratio

129   between the planar area of buildings and the lot area) λ_p from 0.028 to 0.69 were

130   considered. The cube height H was equal to 0.06m. The lot area was a square with a

131   side length of $13H$ (0.78m) (see Fig. 3a later in the text).

132   Drag force and pressure measurements were performed separately on one individual

133   cube ("target cube" hereinafter) placed along the middle column of the array (Fig. 1b).

134   Please note than when the number columns was even (as for example for λ_p=0.0625 in

135   the figure), the measurements were performed along one of the two columns

136   constituting the middle of the array. The target cube was kept fixed on the wind tunnel

137   floor while its position within the array was changed by moving the other cubes.

138   Initially the target cube was located in the first row. In the next step the cubes from the

139   last row were moved to the front so that the target cube was located in the second row

140   of the array. This procedure was repeated until the target cube was positioned in the last

141   row of the array.

142   The employed geometries are the same as used in our previous paper (Buccolieri et

143   al., 2017), i.e. the lot area was kept constant (the denominator in λ_p) and the number of

144   cubes was increased to represent neighbourhoods of different λ_p. In this approach there

145   may exist conditions where flow adjustment occurs and conditions where the flow is

146   still evolving. These experiments intend to reproduce conditions in which the

147   surrounding terrain is almost uniform and there is a considerable transition from a given

148   roughness to a new roughness where the flow within the array may be still evolving.
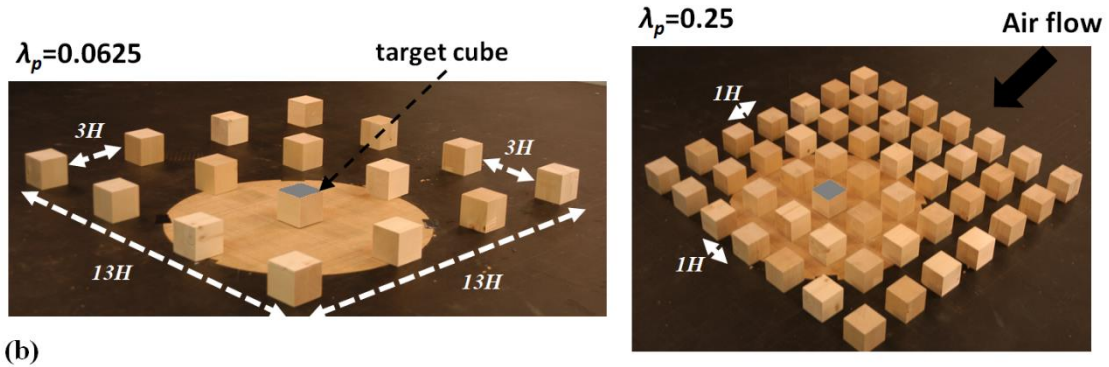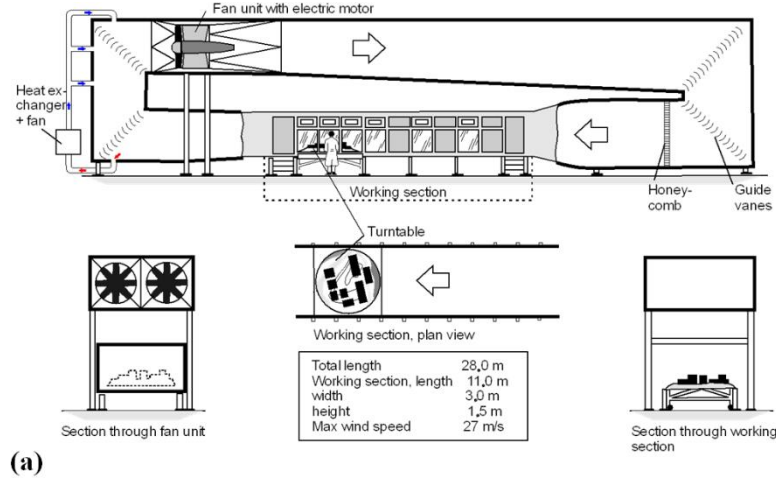
149

Fig. 1 a) Sketch of the wind tunnel. b) Example arrays with planar area index λ_p=0.0625 and
0.25, with indication of air gap between cubes and the target cubes (roof s highlighted in grey)
placed in the centre of the turntable along the centre of the arrays.

2.2. The boundary-layer flow

A boundary-layer (BL) flow in the wind tunnel was achieved considering two

different conditions for the fetch: (i) the entire fetch was covered with cubes of 0.04m

side length representing roughness elements ("BL roughness" hereinafter); (ii) the fetch

was smooth with no roughness elements ("BL no roughness" hereinafter). The distance

between the final row of roughness elements and the front of the lot area was

approximately 0.4m. The roughness area in the working section of the wind tunnel had

a total length of 8m made of spires in the first part and then of 0.04m cubes (roughness

elements).

The boundary layer thickness δ was about 0.15m (2.5H) in the "BL no roughness"

case and about 0.8m (13.3H) in the "BL roughness" case, as estimated by taking the

height at which the velocity was equal to 99% of the free stream velocity. The blockage

coefficient ($\Phi = A_{model,proj.}/A_{wind\_tunnel}$, where $A_{model,proj.}$ [m^2] is the projected area of the

cube along the main wind direction and A_{wind_tunnel} is the cross-sectional area of the

6

169   measurement section in the wind tunnel), was about 0.1% which fulfils the requirements

170   of the VDI 3783 guidelines (2004).

171   The experiments were performed with one reference wind velocity $U(H)$ [ms^{-1}] at the

172   cube height H, corresponding to 500 revolutions per minute (rpm) of the fan that drove

173   the flow in the wind tunnel. The independence of the drag force on the reference

174   velocity was tested in the previous work (Buccolieri et al., 2017). The error is within

175   ±5% of the measured value. Undisturbed mean velocity and relative turbulence intensity

176   profiles approaching the array (which are in equilibrium with the roughness in the

177   fetch), both normalised by the corresponding value at H=0.06m up to z/H=2.5, are (Fig.

178   2):

179
$$\frac{U(z)}{U(H)} \approx \left(\frac{z}{H}\right)^{0.16} \tag{1}$$

180
$$\frac{I(z)}{I(H)} \approx \left(\frac{z}{H}\right)^{-0.06} \qquad \text{(BL roughness)} \tag{2}$$

181
$$\frac{I(z)}{I(H)} \approx \left(\frac{z}{H}\right)^{-0.46} \qquad \text{(BL no roughness)} \tag{3}$$

182
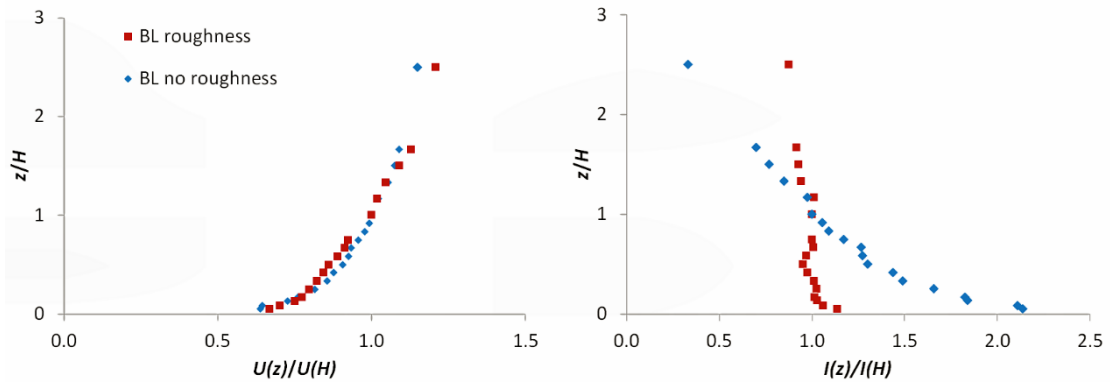
183
184
Fig. 2 a) Boundary layer (BL) wind velocity (left) and relative turbulence intensity (right)
185   incoming profiles in the wind tunnel for rpm = 500. The profiles have been fitted using power
186   laws in Eqs. 1, 2 and 3.

187

188   The velocity was measured with a TSI hot-film anemometer in the middle of the

189   empty circular disk where the target cube was attached (see subsection 2.3). The

190   turbulence intensity was calculated as the standard deviation of the velocity fluctuations

191   divided by the mean velocity. Tab. 1 summarizes the cases investigated.

192

193

194 **Table 1**
195 Summary of all test cases investigated in the wind tunnel. *U(H), I(H)* and *Re* are the incoming
196 mean flow velocity and turbulence intensity at building (cube) height *H* and the Reynolds
197 number, respectively.

No. of cubes	λ_p	Air gap between buildings (in the transversal and longitudinal directions)	Centre to centre distance between buildings (in the transversal and longitudinal directions)	$U(H)$ [ms^{-1}] - $I(H)$ [%] – Re [-]	
1	-	Isolated cube		**BL roughness**	**BL no roughness**
3x3	0.028	5*H*	6*H*	5.2 - 27.6 - 20,800	9.5 - 7.1 - 38,000
4x4	0.0625	3*H*	4*H*		
5x5	0.11	2*H*	3*H*		
7x7	0.25	1*H*	2*H*		
9x9	0.44	0.5*H*	1.5*H*		
10x10	0.56	0.33*H*	1.33*H*		
11x11	0.69	0.2*H*	1.2*H*		

198 *Note: the Reynolds number, based on the height of the cube H and the incoming undisturbed*
199 *reference flow velocity U(H) at cube height H, is lower in the "BL roughness" case as a*
200 *consequence of the smaller U(H).*
201

202 ### *2.3. Drag force measurements*

203 The drag force F_D (balance) acting on the individual target cube was directly

204 measured using the standard load cell method described in Buccolieri et al. (2017).

205 Specifically, the target cube was connected to the load cell via two thin rods that went

206 through a small opening in the turn table. There was an air gap of 1mm between the

207 cube and the turn table. The load cell was mounted on a stable tripod standing on the

208 floor of the laboratory hall (Fig. 3) so that the cube was mechanically isolated from the

209 wind tunnel and the measured force was only due to air resistance. To measure the drag

210 force distribution within the array, the force was singularly measured on the cubes

211 located along the centre of the array (along the wind direction).

212 In the standard load cell the horizontal force, caused by the air movement, was

213 transformed into vertical tensile and compressive force at its edges. Here it was Vetek

214 108AA with glued strain gauges (Vetek, 2016) which measured the forces and provided

215 an electrical output signal. The signal was then amplified through the Amplifier,

216 converted to digital through the 16 bit AD-converter and finally read by the Lab View

217 program (Fig. 3). In the program the signal offset (zero) and gain could be adjusted

218 before further processing. The signal from the load cell was sampled at 1000Hz and

219 then a mean value was calculated every second. Due to turbulence the measuring signal

220 still fluctuated and further signal processing was necessary. To obtain stable

8

measurements a sliding average was considered using 60s. The force was read when the
sliding average was stable.

The load cell measured the force along the flow direction since it was mounted in
parallel with the main wind flow. The load cell had an internal compensation that
balances out the torque. Therefore, it measured the net force in the flow direction
regardless of where the force acted on the cube. The accuracy was tested and the total
measurement uncertainty is specified as the reading $\pm$ 7%. Further details, including the
calibration procedure, are given in Buccolieri et al. (2017).
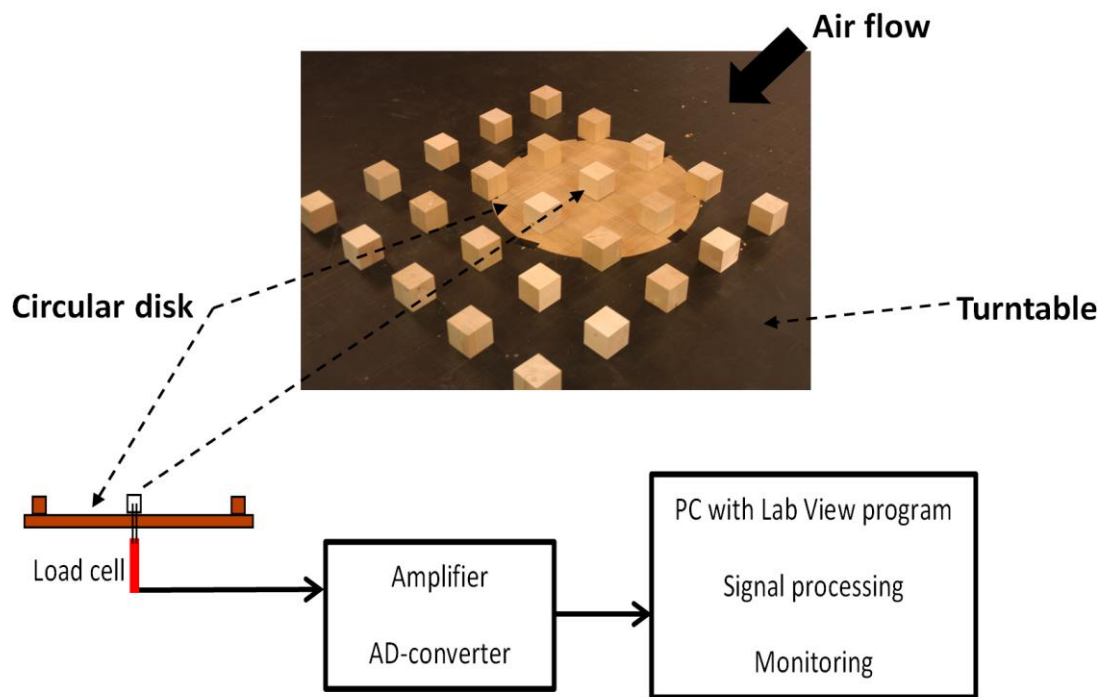
Fig. 3 Pictures showing an example of the array built in the wind tunnel and attached to the
circular disk, with indication of the target cube connected to the load cell.

2.4. Pressure measurements and drag force estimation

The static pressure at windward and leeward sides was measured via pressure taps
placed at the façades of the target cube (Fig. 4a,b). The diameter of the tap openings
was 0.8mm and the opening was oriented perpendicular to the wall. The pressure was
measured only at one half of the façades. All pressure taps were connected to a
multiplexer (scanner valve), which transferred each pressure to the Furness FCO12
pressure transducer. The signal was sampled with 1000Hz and the final reported

9

241   pressure was the average over 30s. The area was then divided into 40 sub-areas (A_i with

242   i=1 to 40) according to where the taps were located (Fig. 4c).

243   The drag force, acting perpendicular on the windward side of the target cube, was

244   then calculated as follows:

245      $$F_{D\_windward}(\text{pressure}) = \sum_{i=1}^{n} p_i \times A_i \tag{4}$$

246   where the measured pressure p_i was assumed to be constant over the entire sub-area A_i.

247   On the leeward side of the target cube (area $A_{leeward}$) the pressure distribution was

248   almost uniform so the force was calculated from the average pressure $p_{average}$ as

249   follows:

250      $$F_{D\_leeward}(\text{pressure}) = p_{average} \times A_{leeward} \tag{5}$$

251   Sensitivity tests using Eq. 4 for calculating $F_{D\_leeward}(\text{pressure})$ showed a percentage

252   difference lower than 2%.

253   The total drag force $F_D(\text{pressure})$ acting on the target cube, along the flow direction,

254   was finally calculated as:

255      $$F_D(\text{pressure}) = F_{D_{windward}}(\text{pressure}) - F_{D_{leeward}}(\text{pressure}) \tag{6}$$

256   The direction of the force was determined by the sign of the pressure.

257
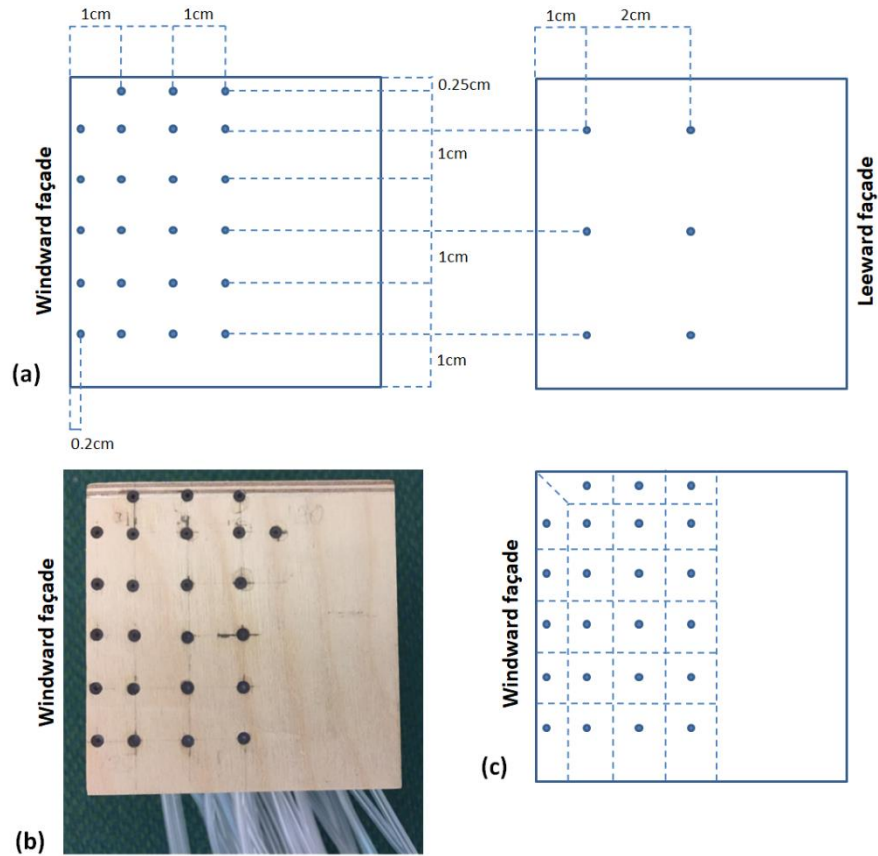
Fig. 4. a, b) Pressure taps position at windward and leeward façades of the target cube. c) Sub-areas of the windward façade employed for the calculation of the drag force via the pressure-derived method.

It should be noted that Eq. 6 represents an integration based on a finite number of sampling points. One can expect the result to be dependent on the number of sampling points and the location of the sampling points, since due to the acceleration of the air flow towards the edges, on the windward side of the building the static pressure varies a lot across the surfaces (see. Fig. 9 later in the text). Therefore, as shown in Fig. 4a, after several tests (not shown here) with different number of sampling points on both the windward and leeward façades, some pressure taps were also placed near the edges of the wall, resulting in good agreement between the calculated (by the pressure-derived method) and measured (with the balance) drag force (see Fig. 7 later in the text).

3. Drag area and cross ventilation

3.1. The drag area

11

277   The drag coefficient based on the drag force F_D generated by the target cube, the

278   reference velocity $U(H)$ and the physical frontal area of the cube A_{Cube} is defined as:

279    $$C_D = \frac{F_D}{\frac{1}{2}\rho U(H)^2 A_{Cube}} \qquad (7)$$

280   With the aim of determining the effective area of cubes generating the drag force, we

281   use the definition of the drag area (Buccolieri et al., 2017) by setting the drag coefficient

282   equal to 1 and solving for the area. The drag area of the target cube (A_D) becomes:

283    $$A_D = \frac{F_D}{\frac{1}{2}\rho U(H)^2} \qquad (8)$$

284   The rationale for introducing a drag area is that it can be compared with the physical

285   area of the cubes in the array. The drag coefficient becomes the ratio between the drag

286   area and the physical area of the cube:

287    $$C_D = \frac{A_D}{A_{cube}} \qquad (9)$$

288   Regarding the magnitude of the drag area there are two extreme cases:

289   *Long distance between the cubes (low λ_p) – No interference between the cubes*

290   The cubes behave as independent bodies and the total drag force acting on the whole

291   array (F_{D_total}) is equal to the number of cubes N multiplied by the drag force F_D

292   generated by the single target cube:

293    $$F_{D\_total}(\text{for low } \lambda_p) = NF_D \qquad (10)$$

294   which, by Eq. 8, leads to the total drag area of the array (A_{D_total}):

295    $$A_{D\_total}\left(\text{for low } \lambda_p\right) = \frac{F_{D_{total}}}{\frac{1}{2}\rho U(H)^2} = N\frac{F_D}{\frac{1}{2}\rho U(H)^2} = NA_D \qquad (11)$$

296   *Short distance between the cubes (large λ_p) – Strong interference between the cubes)*

297   The extreme case is when total force F_{D_total} is on the cube at the front ($F_{D\_front\_cube}$)

298   which, by Eq. 8, leads to total drag area:

299    $$A_{D\_total}\left(\text{for large } \lambda_p\right) = \frac{F_D}{\frac{1}{2}\rho U(H)^2} = \frac{F_{D\_front\_cube}}{\frac{1}{2}\rho U(H)^2} = A_{D\_front\_cube} \qquad (12)$$

300   To generalize, if F_D^i is the drag force generated by cube i within the array and A_D^i is

301   the corresponding drag area, the total drag force exerted by the whole array is equal to:

302    $$F_{D\_total} = \sum_{i=1}^{N} F_D^i \qquad (13)$$

303   and the total drag area A_{D_total} (see Eq. 8) becomes:

$$A_{D\_total} = \frac{\sum_{i=1}^{N} F_D^i}{\frac{1}{2}\rho U(H)^2} = \sum_{i=1}^{N} A_D^i \qquad (14)$$

By dividing the total drag area by the total physical frontal area for each λ_p, $\frac{A_{D\_total}}{\text{Frontal area}}$, it can be evaluated which is the most appropriate reference area (drag area) to be used for the calculation of the drag coefficient C_D, i.e. when the ratio tends to one.

3.2 Assessment of wind-driven cross ventilation based on the drag force

Wind-driven natural ventilation of buildings occurs either as cross ventilation or single-sided ventilation (Etheridge and Sandberg, 1996). Single- sided ventilation occurs when all openings are located on one side (Warren, 1977). Cross ventilation occurs when there are openings on different sides of a building.

Cross ventilation has been studied by several authors using different approaches. Some examples are provided by Karava et al. (2007, 2011), Chu and Chiang (2014) and Shetabvish (2015). More recently Shirzadi et al (2018) have investigated cross ventilation for buildings embedded in arrays using computational fluid dynamics. When the pressure inside the building is uniform (Kobayashi et al., 2010), cross ventilation is assumed to be driven by the difference of the static pressure between outside and inside of the building which generates a velocity through the openings. If the building is a bluff body, the drag force is generated by the pressure difference between the windward and the leeward façades .

In the present paper, in order to assess the potential for cross ventilation it is assumed here that the cubes in the investigated arrays are provided with two openings opposite to each other (Fig. 5) and for simplicity the area of both openings are taken to be equal. By entrainment into the air stream flowing into the room there is a gradual expansion of the air stream. If the distance L, to the leeward wall, is larger than about six times the linear dimension of the opening, the cross section of the air flow have expanded so it is larger than the opening in the leeward wall. Then the whole air stream cannot continue straight through the opening on the opposite side. This is the prerequisite for the pressure inside the building to be uniform.
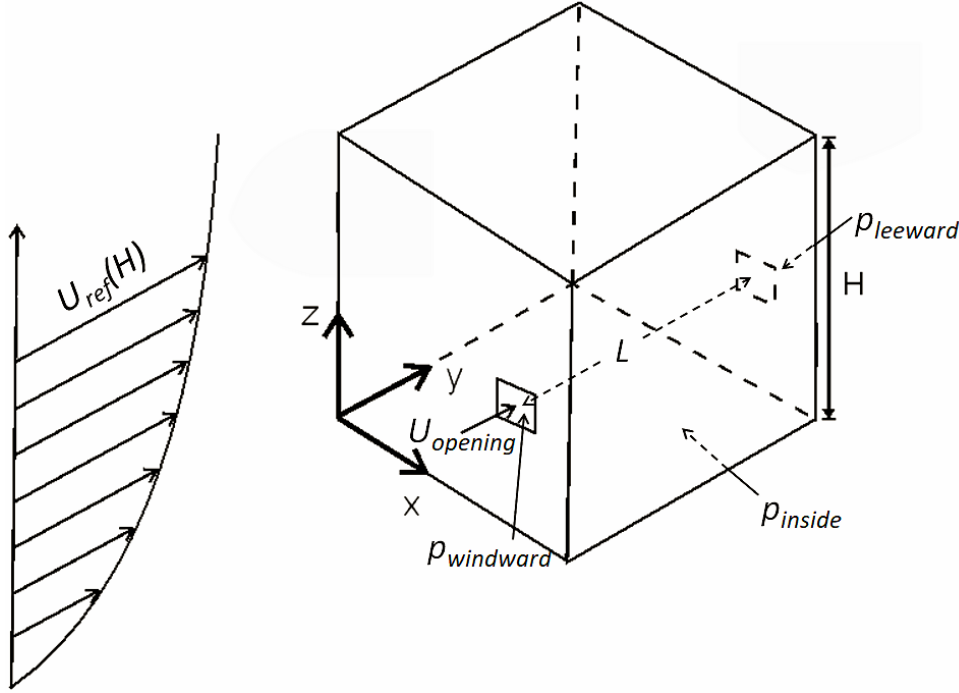
Fig. 5. A cube with two openings located opposite to each other.

The flow rate $Q_{opening}$[m^{3}s^{-1}] through the opening is, by assuming that the velocity
profile is uniform across the opening, given by:

$$Q_{opening} = A_{opening}U_{opening} \tag{15}$$

The velocity in the opening, $U_{opening}$, is driven by the pressure difference $|\Delta\bar{p}_{Out-In}|$
between outside of the building and the inside of the building according to the orifice
equation (Etheridge and Sandberg, 1996):

$$U_{opening} = C_{discharge}\sqrt{\frac{2|\Delta\bar{p}_{Out-In}|}{\rho}} \tag{16}$$

where $C_{discharge}$ is the discharge coefficient which takes into account several factors as
e.g. area contraction of the stream tube when passing through the opening and losses.

For the opening on the windward façade $\Delta\bar{p}_{Out-In} = (\bar{p}_{windward} - \bar{p}_{inside})$ and for
the opening on the leeward façade $\Delta\bar{p}_{Out-In} = (\bar{p}_{inside} - \bar{p}_{leeward})$. The unknown
quantity is the pressure $\bar{p}_{inside}$ within the cube which we assume to be constant within
the cube. This condition is fulfilled if the openings are not too large. The pressure
variation inside a building related to the size of the openings is shown in Kobayashi et
al (2010). This pressure inside the cube is obtained from the flow balance that dictates
that the flow rates through both openings are the same. For simplicity, we set the

discharge coefficients for the openings on the windward and the leeward façades the
same. This implies that the pressure difference across both openings is the same and the
pressure within the cube is equal to the average of the pressure on the windward and the
leeward façades. Therefore, the pressure difference across both openings becomes equal
to half the pressure difference between the leeward and the windward side:

$$\Delta\bar{p}_{Out-In} = \frac{1}{2}\left(\bar{p}_{windward} - \bar{p}_{leeward}\right) \tag{17}$$

This pressure difference can be assessed from the drag force F_D(balance) measured
with the standard load cell and the physical surface area of the cube F_D(balance) as
follows:

$$\left(\bar{p}_{windward} - \bar{p}_{leeward}\right) \approx \frac{F_D(\text{balance})}{A} \tag{18}$$

Inserting this into Eq. 16 the velocity through the opening $U_{opening}$ in relation to the
reference velocity $U(H)$ can be written as:

$$\frac{U_{opening}}{U(H)} = \frac{C_{discharge}\sqrt{\frac{F_D(\text{balance})}{\rho A}}}{U(H)} \tag{19}$$

The discharge coefficient $C_{discharge}$ reported in the literature varies a lot. This is due
to that apart from different conditions at the tests, the discharge coefficient takes into
account many factors. In many practical applications the discharge coefficient is an
adjustment factor that links flows at complex conditions to the orifice equation.
According to Karava et al. (2004) the discharge coefficient varies between 0.14-0.65
and according to Cruz and Viegas (2016) it varies between 0.47-0.81. In our assessment
a precise estimation of the discharge coefficient is not available and thus we set it equal
to 1 because the whole analysis is only an order of magnitude estimate. This implies
that we, if the orifice equation is valid, overestimate the potential. After setting the
discharge coefficient equal to 1, Eq. 19 leads to:

$$\frac{U_{opening}}{U(H)} = \frac{\sqrt{\frac{F_D(\text{balance})}{\rho A}}}{U(H)} = \frac{1}{\sqrt{\rho A}}\frac{\sqrt{F_D(\text{balance})}}{U(H)} \tag{20}$$

Please note that if an estimate of the discharge coefficient is available, this can the
easily be taken into account by multiplying Eq. 20 by the new discharge coefficient and
the results will be qualitatively similar to those presented in subsection 4.4 (see Fig. 10
later in the text).

380   Eq. 20 is used here to evaluate the potential for cross ventilation driven by a static

381   pressure difference. The façade area $A = H^2$ is constant while the reference velocity at

382   roof height $U(H)$ is dependent on the type of boundary layer generated (roughness

383   elements in the fetch or not). According to Eq. 20 the velocity in the opening $U_{opening}$

384   approaches zero when the force approaches zero, which occurs when the difference in

385   mean pressure (Eq. 18) approaches zero. Now other mechanisms for exchange of air

386   between the interior of the building and the ambient come into play (Haghighat et al.,

387   1991). One mechanism is the penetration of turbulent eddies through the openings and

388   another one is flow driven by pressure fluctuations. Pressure fluctuations are generated

389   by e.g. vortex shedding (Zu and Lam, 2018). These mechanisms give rise to penetration

390   phenomena with strong variations in time and therefore the exchange between the

391   indoor and the ambient cannot always be estimated from the flow rate in the opening

392   based on the velocity field (air exchange rate). Instead the exchange must be based on

393   an exchange of a passive contaminant present indoor. This exchange is retained from

394   concentration data. This exchange rate is the purging flow rate (Etheridge and

395   Sandberg, 1996) and is maximized by the air exchange rate. An example of predicting

396   the purging flow rate from concentration data can be seen in Kobayashi et al (2018).

397   It should be noted that there is a direct relation between the velocity in opening

398    $U_{opening}$ according to Eq. (20) and the assessment of the in-canopy velocity U_C

399   according to Bentham and Britter (2003) relation (2):

400    $$U_C = \sqrt{2} U_{opening} \qquad\qquad (21)$$

401   This relation is obtained from the relation (2) in Bentham and Britter (2003) by

402   substituting the left hand side with the drag force and in the right hand side setting the

403   drag coefficient equal to 1. Eq. 21 implies that it is possible to read off the variation in

404   in-canopy velocity from the variation in the velocity through an opening and vice versa.

405

406   **4. Results**

407   *4.1. Evaluation of the drag distribution*

408   *4.1.1 Interaction between the approaching flow and the array*

409   Fig. 6a shows a sketch of the flow pattern when the wind approaches the array. For

410   the approaching wind the array constitutes a resistance consisting of a blockage by

411   cubes generating a drag force, while for the air stream passing through the street

412   canyons the resistance is generated by a friction against the surfaces forming the street

413   canyons. At the frontal façades of cubes there are stagnation points and for the air

414   stream passing along the street canyons there are corresponding retardment points

415   defined as the points with the highest static pressure (Sandberg et al., 2004). Due to the

416   increased resistance only a fraction of the approaching flow can penetrate into the array

417   because the street canyons have a lower flow capacity (Hang et al, 2010) than the

418   surrounding non occupied terrain. The fraction (dashed line in the figure) that does not

419   entrain into the array continues above the array. At the downstream end of the array

420   there is a corresponding change from a higher to a lower resistance that causes the flow

421   capacity downstream to increase. This change generates a downward flow at the

422   downstream end of the array. Fig. 6b shows the evolution of the static, dynamic and

423   total pressure in the approach flow continuing through the street canyon.
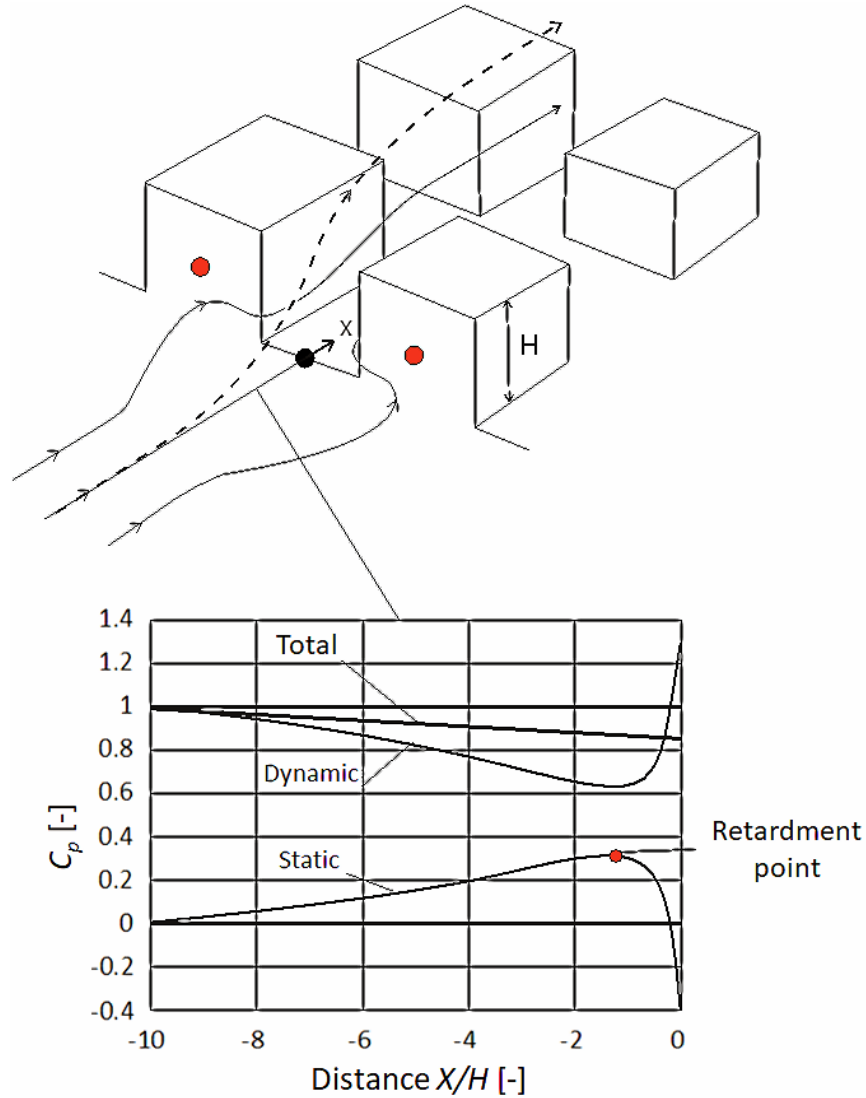
424

Fig. 6. Flow towards the cubes in the front row. a) Sketch of the flow pattern and b) pressure coefficient by static, dynamic and total pressure along the line indicated in a) (adapted from Sandberg et al., 2004).

4.1.2 Interaction between the cubes and the boundary layer

For an isolated cube a shear boundary layer is developed and by flow separation a characteristic flow pattern is generated around the cube with a wake on the leeward side. With respect to a reference pressure the isolated cube experiences a positive pressure on the windward side and a negative pressure in the wake on the leeward side. The difference between these pressures generates a drag force on the cube. For an array of cubes, the introduction of surrounding cubes creates an air gap around all cubes located within the interior region of the array. The air gaps constrain the flow and consequently the windward and leeward pressures to be changed relative to an isolated

439 cube. There are many physical phenomena that may affect the drag force on individual
440 cubes which depends on their location within the array. The velocity in the wake is less
441 than the free stream velocity and therefore the cube behind the first cube will be
442 sheltered and subsequently exposed to a lower velocity than the first cube. The result is
443 a lower drag force. If the cubes come very close to each other the cube downstream will
444 be fully submerged within the wake of the first cube which results in a force directed
445 opposite to the wind direction. The second cube may also affect the cube upstream by
446 that the location of the point of separation on the sides of the upstream cube is changed.
447 If the cubes are very close to each other there may be no separation from the first cube.

448   The introduction of surrounding cubes will thus lead to an interference. Based on
449 field measurements and modelling results, Oke (1988) identified three flow regimes for
450 wind direction perpendicular to the street axis in neutral stratification. For widely
451 spaced buildings (aspect ratio between the building height H and the street width W <
452 0.3), the flow fields associated with the buildings do not interact (isolated roughness
453 flow regime). At closer spacing (0.3<H/W<0.7) the wake behind the upwind building is
454 disturbed by the recirculation created in front of the windward building (wake
455 interference flow regime). Further reducing spacing (H/W>0.7) results in the skimming
456 flow regime, where a stable recirculation is developed inside the canyon and the
457 ambient flow is decoupled from the street flow.

458   The degree of interference can be expressed as an "interference factor" defined as
459 $F_D/F_{D\_isoltaed\_cube}$, i.e. the ratio between drag force of the target cube surrounded by
460 cubes and the drag force generated by an isolated cube. There are thus three cases: 1) no
461 interference (interference factor = 1); 2) Sheltering (interference factor < 1); 3)
462 Amplification (interference factor > 1).

463

4.1.3 Measured drag distribution

465   Fig. 7 shows the interference factor for the cases with a boundary layer generated
466 with roughness elements in the fetch. The cases with a boundary layer generated with
467 no roughness elements in the fetch exhibit a similar behaviour. Both the drag forces
468 measured by the balance and the pressure difference are presented. The balance
469 measured the total contribution to the drag due to the form drag and friction. By

470 definition the drag based on the pressure difference is the form drag. The cube is a bluff
471 body so we expect the form drag to dominate.

472 From the figure it can be argued that the standard load cell method and the pressure-
473 derived method provided similar distribution of the drag force within the array. This
474 provides confidence in the measurements. Only the target cube located at the first row
475 showed a normalized drag force based on the pressure about 10% larger than the drag
476 force based on measurements by the balance. It is likely that this difference is due to
477 that the pressure is measured in a finite number of points. Secondly, results confirm that
478 the change in distribution of the drag force when changing the building packing density
479 is in accordance with assessment of the distribution of the drag force based on
480 measurements of the total drag force of the whole array reported in (Buccolieri et al.,
481 2017). For further details see also the next subsection.

482 At the lowest packing density λ_p=0.028 (air gap between the cubes is $5H$) there is no
483 interference. And at λ_p=0.11 (air gap $2H$) the interference factor is 0.5, while at λ_p=0.25
484 (air gap $1H$) the force is almost totally exerted by the first cube. As discussed in
485 Buccolieri et al. (2017) the latter case corresponds to a maximum drag force generated
486 by the whole array (see Fig. 6 of their paper). With further increase of λ_p, the drag force
487 slightly decreases until it becomes almost constant. One can claim that at λ_p=0.25 the
488 array start to behave as one single unit. The effect of an increase of the frontal area is in
489 fact cancelled out by the reduction of mean wind velocity (see Buccolieri et al., 2010).
490 At λ_p=0.44 the air gap is $0.5H$ and the drag force on the cube located downstream of the
491 cube at the front of the array becomes negative. We interpret this as that the second
492 cube now is submerged (Gowda and Sitheeq, 1990) in the boundary layer generated by
493 the cube at the front. However it remains to verify this by flow visualization. A further
494 detail is that starting with λ_p=0.11 the drag force on the cube at the front is less than on
495 an isolated cube. This we interpret as that the cube downstream affect the drag force
496 exerted on the cube at the front. However for the largest packing density λ_p=0.69 (air
497 gap $0.2H$) there is an amplification of the drag force on the front cube in the row that we
498 cannot explain. Associated with the change in the distribution of the drag force with
499 changing packing densities there is a change in the air flow pattern. In Figure 7 of
500 Buccolieri et al (2010) it is shown that starting from packing density λ_p=0.44 there are
501 recirculation zones within the array.
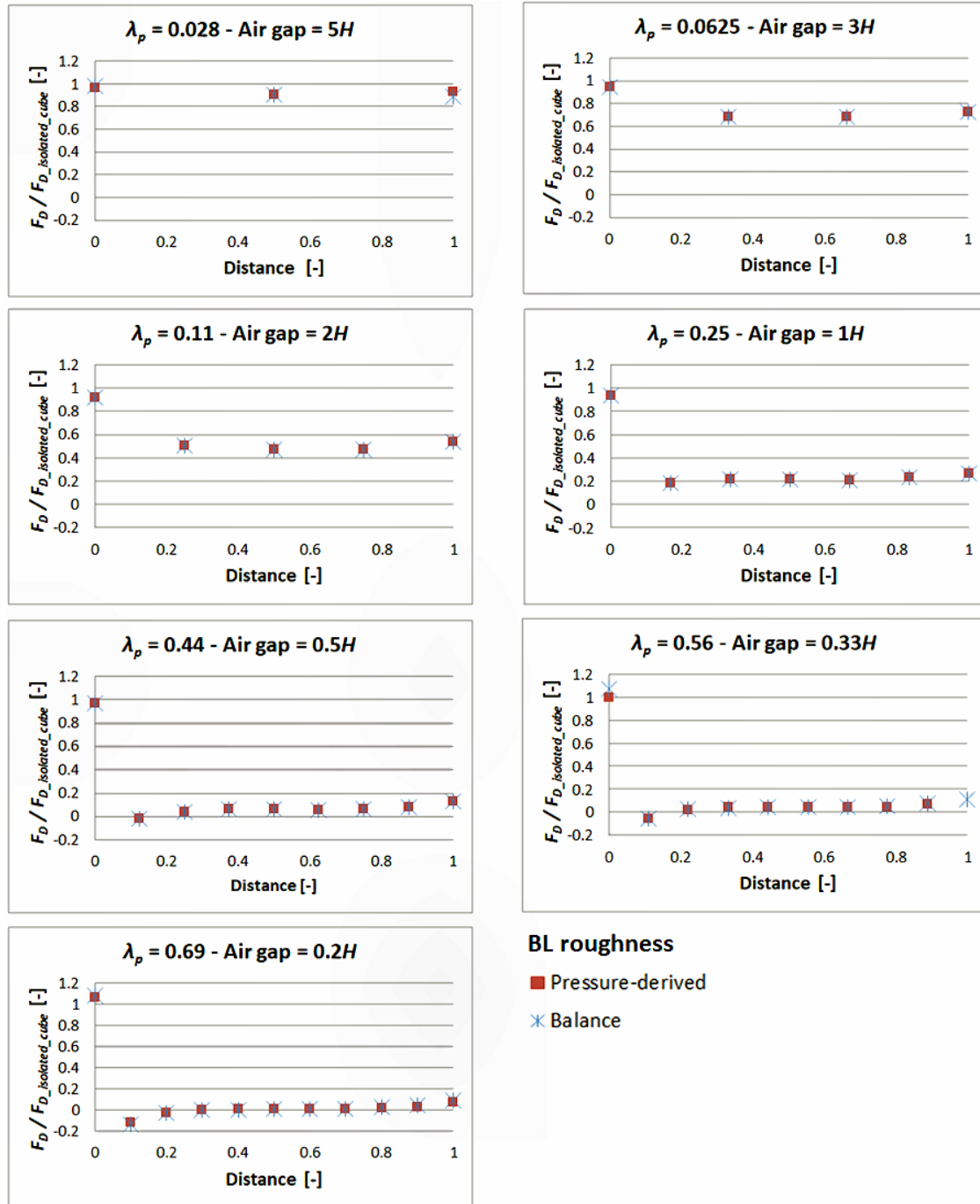
502

503
504 **Fig. 7**. Profiles of $F_D / F_{D\_isolated\_cube}$ (interference factor) generated by the target cubes, BL
505 roughness case. The x-axis represents the distance from the first target cube of the array ("0") to
506 the last target cube ("1"), see Fig. 1.
507

4.2. Assessment of the drag area

508

509   In Buccolieri et al (2017) the drag area distribution was assessed from the total drag
510 force recorded over the whole array by calculating the ratio: Total drag area/Frontal

21

area, i.e. the ratio between the total drag area retrieved from the total drag force and the

physical frontal area of the whole array (see their Eq. 13).

Here the same relation is employed but using the drag force measured on the

individual target cube. The total drag area is thus estimated by adding the drag forces

measured with the balance generated by the single target cubes and the physical frontal

area is the total frontal area of the target cubes. Two extreme cases of the frontal area

are chosen, i.e., the physical frontal area of all the middle column of the array and the

physical frontal area of the first (upstream) target cube. Each cube has a frontal area

equal to $0.036m^2$.

The comparison is shown in Fig. 8. First it can be noted that the drag distribution

obtained from current measurements on individual cubes is similar to that obtained from

measurements over the whole array. This suggests that, when estimating the drag area

generating the drag force, the single middle column is representative of the whole array

for each λ_p, indicating that our choice of isolated array well represents the drag force

exerted by a portion of the city of a given λ_p. Second the figure shows that, as expected

by the drag force distribution shown in Fig. 7, for low packing density the total frontal

area is the most appropriate reference area (drag area) since the ratio is close to one,

whereas for large packing densities the frontal area of the first row only is the one to be

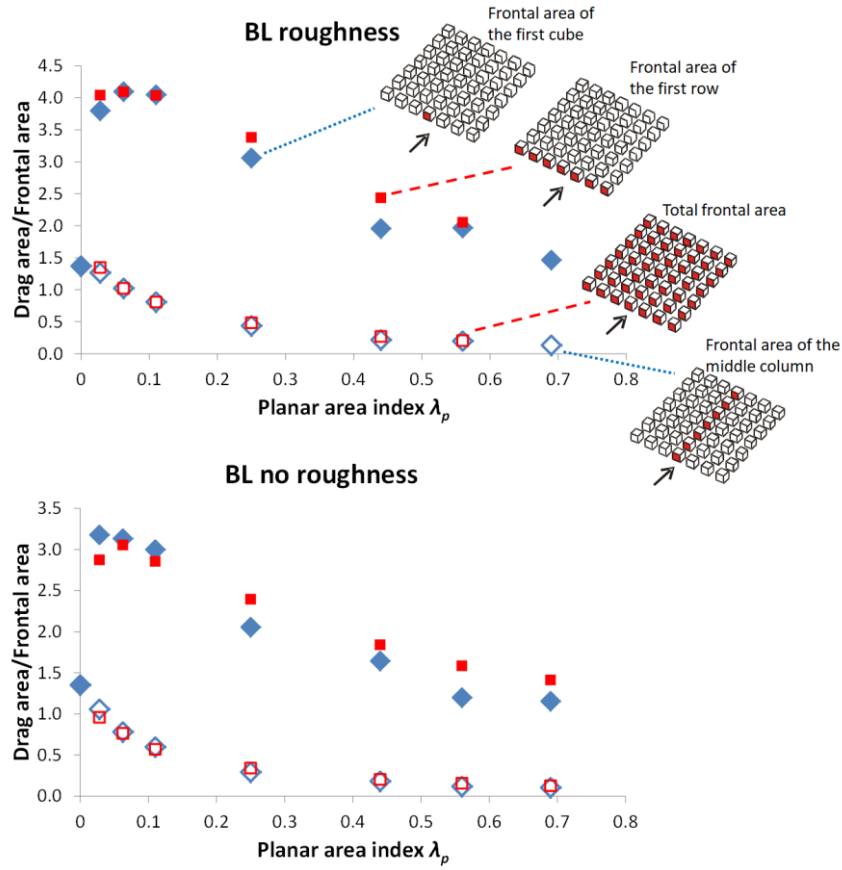used as the appropriate reference area.

Fig. 8. Drag area/Frontal area as a function of the planar area index λ_p when using the frontal area of the first cube or of the first row of cubes (full rhombus and square, respectively) and the frontal area of the middle column or of all the cubes (empty rhombus and square, respectively) in the a) ''BL roughness'' and b) ''BL no roughness'' cases. Note: square symbols refer to drag force measurements over the whole array (Buccolieri et al., 2017).
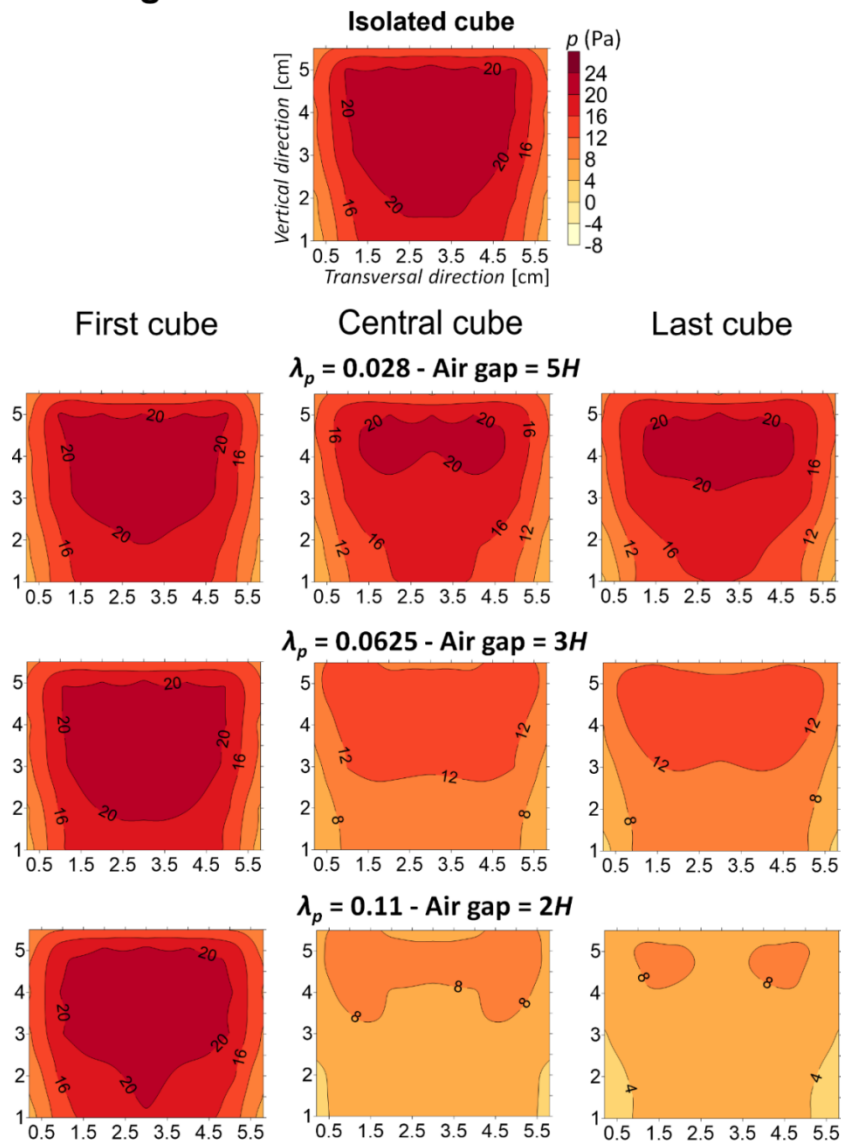
4.3 Pressure distribution on the surface of target cubes

To show the spatial distribution of pressure, Fig. 9 shows the pressure contours on the windward side of the first, central and last target cubes for the BL roughness case obtained by interpolating the measured pressure. Results for the BL no roughness follow a similar behaviour. We remind here that the pressure was measured (i) on the same target cube as the drag force was measured by the balance; and (ii) on one half of the side only (see Fig. 4), and therefore eventual asymmetries in the horizontal direction is not revealed which of course is a limitation. The stagnation point is the point with the highest pressure and from this point the air approaching the façade is distributed over the façade. For an isolated cube the stagnation point lies on the vertical symmetry line. However when a cube is lying in the front row of an array the location of the stagnation

549   point is probably affected by the amount of air pressed into the street canyon, formed by

550   two neighboring rows.

551   Fig. 9 shows that for all packing densities the first cube (i.e. the cube at the upstream

552   first row of the array) has qualitatively the same pressure distribution as for the isolated

553   cube. Further, the pressure distribution for the lowest packing density (λ_p=0.028) is

554   qualitatively similar for all cubes in the row, that is the interference between the cubes

555   is low in this case. This is in contrast to the case with the highest packing density

556   (λ_p=0.69) where the pressure distribution on the cube at the centre and at the end of the

557   row is almost uniform. The general trend is that with increasing packing density the

558   gradient of the pressure distribution on the wall diminishes for the central and last

559   cubes. This is due to the fact that with increasing packing density the width of the air

560   gap between the cubes diminishes and this constrains the air motion. Because the

561   pressure distribution is a footprint of the air motion along the wall, this results in a more

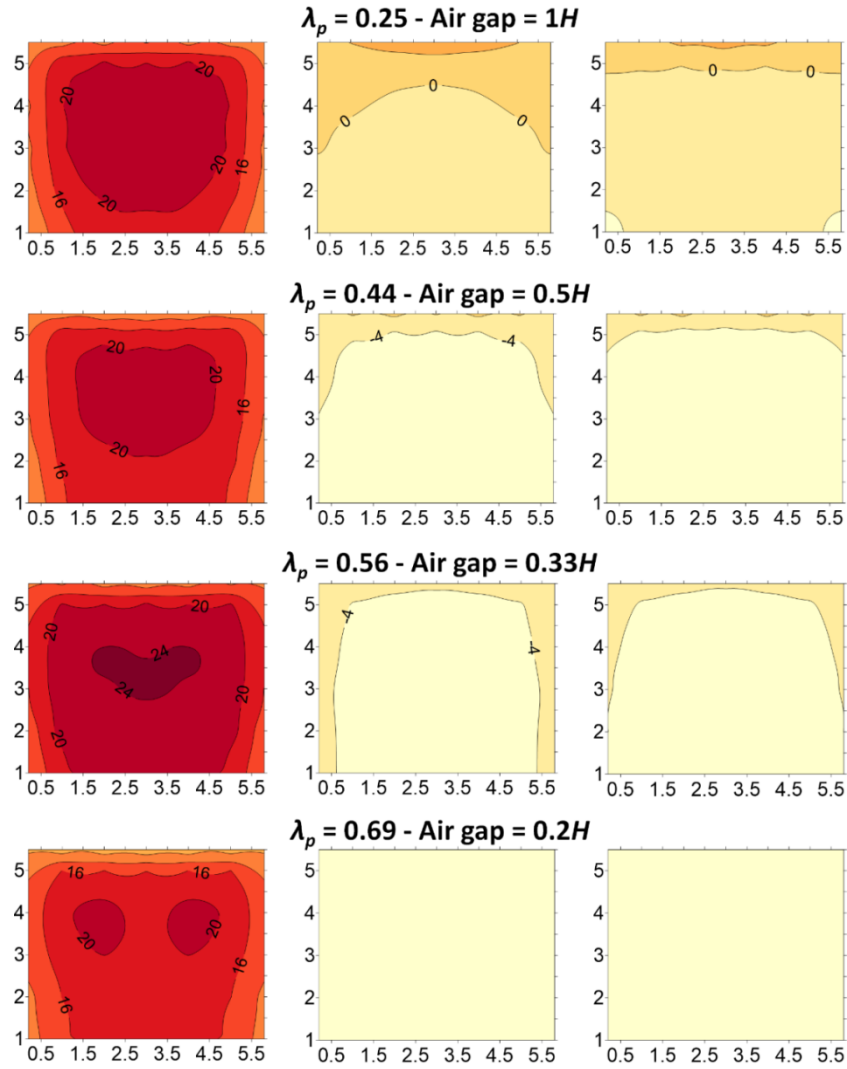562   uniform pressure distribution.

563

BL roughness

Isolated cube

First cube   Central cube   Last cube

$\lambda_p = 0.028$ - Air gap = $5H$

$\lambda_p = 0.0625$ - Air gap = $3H$

$\lambda_p = 0.11$ - Air gap = $2H$

564

Fig. 9. Pressure contours on the windward façade of the first, central and last target cubes for each packing density λ_p, BL roughness case.

4.4. Assessment of the potential for cross ventilation

The potential for cross ventilation is shown in Fig. 10 as the ratio between the velocity at the opening $U_{opening}$ and the reference velocity $U(H)$ at the height of the cube according to Eq. 20. This velocity ratio is dependent on the square root of the drag force multiplied with an expression which only varies with the type of boundary layer, generated either with no roughness elements in the fetch or with roughness elements in the fetch. We remind here that in Eq. 20 the force measured by the balance F_D(balance) is employed.

The figure shows that for the first (upstream) target cube the velocity ratio becomes about the same for both types of boundary layers and is approximately about 0.8.

580   Overall for cubes located downstream the velocity ratio with increasing packing density

581   shows a similar qualitative behaviour as that found for the drag force (see Fig. 7).

582   Specifically, when the packing density is λ_p=0.25 the velocity ratio has dropped to

583   approximately 40% and by further increasing the packing density to λ_p=0.44 the

584   velocity ratio drops to 20%. This shows that, as expected, cross ventilation is very much

585   affected by the packing density. One can expect that single sided ventilation is less

586   sensitive to the packing density because the ventilation is mainly generated by

587   fluctuations. On the other hand single sided ventilation is in general much less than

588   cross ventilation. For the same object the relation between cross ventilation and single

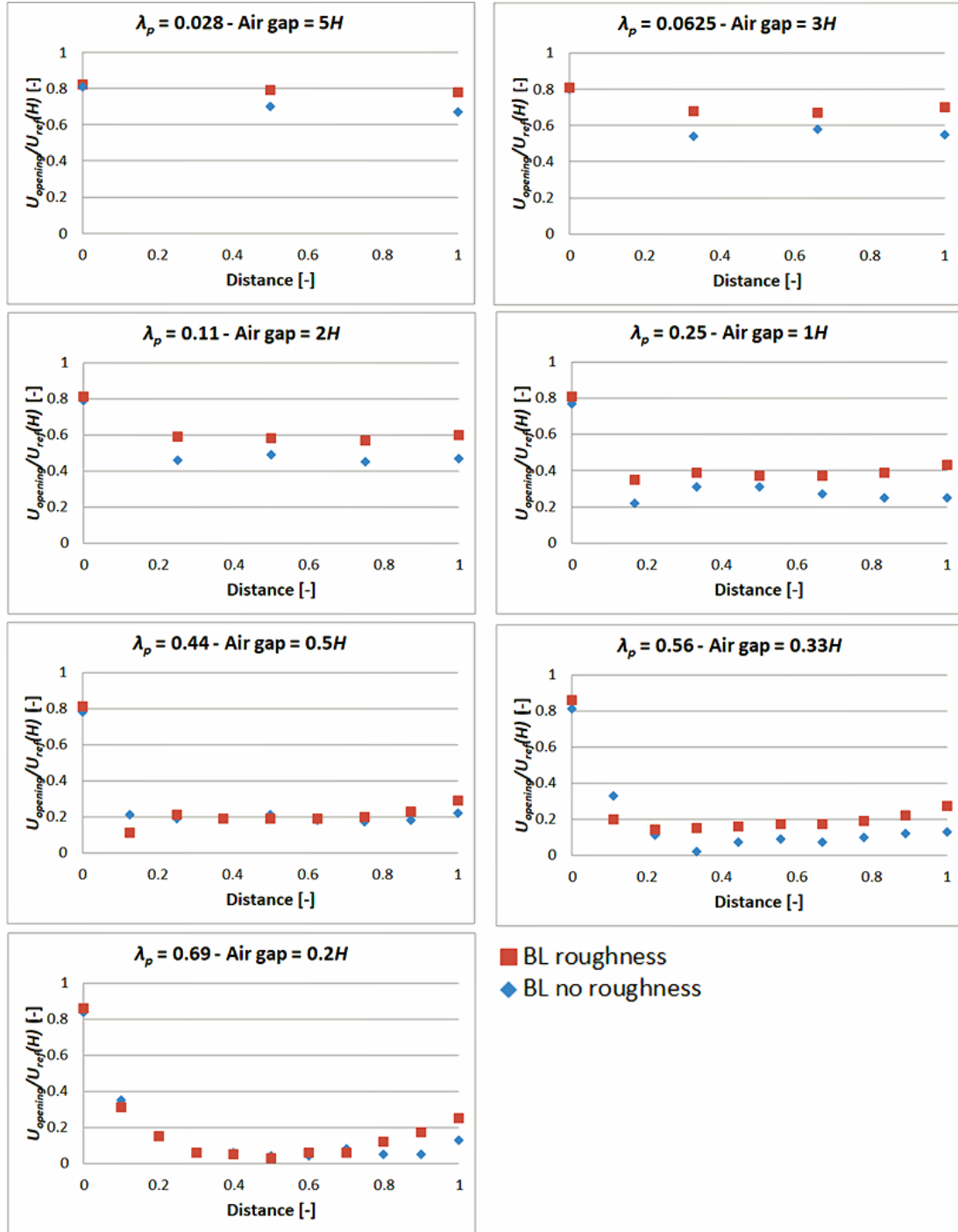589   sided ventilation has been studied in wind tunnel tests reported in Hayati et al. (2018).

590

591
592 **Fig. 10.** Cross ventilation assessment through the ratio of velocity at the opening $U_{opening}$ and
593 the reference velocity $U(H)$. The x-axis represents the distance from the first target cube of the
594 array ("0") to the last target cube ("1") , see Fig. 1.
595

5. Conclusions

596
597   The drag force distribution generated by regular arrays of cubes was measured in a
598 wind tunnel. The force was measured using both a standard load cell and indirectly
599 estimated by measuring the static pressure at windward and leeward façades. The

600 measurements with the two methods coincide within 10%. The drag force is presented

601 as an interference factor by dividing the measured drag force with the drag force from

602 an isolated cube. The main findings of the paper are summarized below:

603 - for the lowest packing density, the drag force is almost uniformly (within 15%)

604 distributed between the cubes within the array. With increasing packing density the

605 force exerted on the fraction of the cubes located downstream of the first row

606 progressively diminishes, and for the highest packing densities the whole force is

607 exerted on the first row, primarily. At the largest packing densities the force on the

608 second row is negative i.e. directed opposite to the wind direction;

609 - as the packing density increases the interaction between the buildings changes from a

610 collection of weakly interfering rows to become a single array, and finally as one row

611 only. This implies that for very low packing densities the total frontal area is the most

612 appropriate reference area (drag area) whereas for large packing densities the most

613 appropriate reference area is the frontal area of the first row;

614 - the methodology previously presented in Buccolieri et al (2017) is further verified

615 demonstrating that the distribution of the drag force within the array can be derived

616 from the total drag force, using a combination of the total drag force expressed as a drag

617 area and the physical frontal area of the cubes.

618 - the potential for cross ventilation is quantified as the velocity through a ventilation

619 opening which is proportional to the square root of drag force. It is shown that there is a

620 direct relation between the velocity through a ventilation opening and the in canopy

621 velocity. This is an observation that has not previously pointed out.

622 - the recorded pressure contours on the façades of the cubes is a footprint of the air

623 motions in the air gap between the cubes showing that with increasing packing densities

624 the gradient of the pressure decreases.

625   Measuring the drag force correctly is not only relevant for the field of wind load on

626 structures, but also for the derivation of improved description of the effect of the city

627 within atmospheric mesoscale models. Several mesoscale studies of the drag force

628 generated by arrays of buildings have been carried out with different methods. For

629 example, Gutierrez et al. (2015) implemented a mechanical drag coefficient formulation

630 depending on packing density following Santiago et al. (2010) into the Building Effect

631 Parameterization + Building Energy Model system coupled with mesoscale Weather

Research Forecasting model. The mesoscale model was applied over New York obtaining an improvement of accuracy of mesoscale model in predicting surface wind speed in complex urban area. We expect that in the future the drag force distribution obtained for different wind directions (providing a sort of "drag force rose"), which may lead to very significant changes in the total drag imposed by the surface (Claus et al., 2012a,b; Santiago et al., 2013), can be the basis for a first order modelling of the dispersion of pollutants within an urban area.

References

1. Antoniou N, Montazeri H, Wigö H,. Neophytou M K.-A , Blocken B, Sandberg M 2017. CFD and wind-tunnel analysis of outdoor ventilation in real compact heterogeneous urban area: Evaluation using "air delay". Building and Environment 126, 355-37.
2. Bentham T., Britter R., 2003. Spatially averaged flow within obstacle arrays. Atmospheric Environment 37, 2037-2043.
3. Buccolieri R, Sandberg M, Di Sabatino S., 2010. City breathability and its link to pollutant concentration distribution within urban-like geometries. Atmospheric Environment 44, 1894-1903.
4. Buccolieri R., Wigö H., Sandberg M., Di Sabatino S., 2017. Direct measurements of the drag force over aligned arrays of cubes exposed to boundary-layer flows. Environmental Fluid Mechanics 17, 373-394.
5. Chen L., Hang J., Sandberg M., Claesson L, Di Sabatino S., Wigo H., 2017. The impact of building height variations and building packing density on flow adjustment and city breathability in idealized urban models. Building and Environment 118, 344-361.

664   6. Cheng H., Castro I.P., 2002. Near wall flow over urban-like roughness. Boundary-
665   Layer Meteorology 104, 229-259.

666   7. Cheng H., Hayden P., Robin A.G., Castro I.P., 2007. Flow over cube arrays of
667   different packing densities. Journal of Wind Engineering and Industrial
668   Aerodynamics 95, 715-740.

669   8. Chu C.-R., Chiang B.-F., 2014. Wind-driven cross ventilation in long buildings.
670   Building and Environment 80, 150-158.

671   9. Claus J., Coceal O., Thomas T.G., Branford S., Belcher S.E., Castro I.P., 2012a.
672   Wind-direction effects on urban-type flows. Boundary-Layer Meteorology 142,
673   265–287.

674   10. Claus J., Krogstad P.-A., Castro I.P., 2012b. Some measurements of surface drag in
675   urban-type boundary layers at various wind angles. Boundary-Layer Meteorology
676   145, 407-422.

677   11. Cruz H., Viegas J.C., 2016. On-site assessment of the discharge coefficient of open
678   windows. Energy and Buildings 126, 463-476.

679   12. Etheridge D.W., Sandberg, M., 1996. Building Ventilation-Theory and
680   Measurement. John Wiley & Sons, Chichester.

681   13. Gowda L.B.H., Sitheeq M.M., 1990. Effect of interference on the pressure
682   distribution on the ground plane around two low-rise prismatic bodies in tandem
683   arrangement. Applied Scientific Research 47,129-149.

684   14. Gutiérrez E., Martilli A., Santiago J.L., González J.E., 2015. A mechanical drag
685   coefficient formulation and urban canopy parameter assimilation technique for
686   complex urban environments. Boundary-Layer Meteorology 157, 333-341.

687   15. Haghighat F., Rao J., Fazio, P., 1991. The influence of turbulent wind on Air
688   exchange rate -a modelling approach. Building and Environment 26, 95-109

689   16. Hamlyn D., Britter R., 2005. A numerical study of the flow field and exchange
690   processes within a canopy of urban–type roughness. Atmospheric Environment 39,
691   3243-3254.

692   17. Hagishima A., Tanimoto J., Nagayama K., Meno S., 2009. Aerodynamic parameters
693   of regular of rectangular blocks with various geometries. Boundary Layer
694   Meteorology 132, 315-337.

695   18. Hang J., Sandberg M., Li Y., Claesson L., 2010. Flow mechanisms and flow
696   capacity in idealized long-street city models. Building and Environment 45, 1042-
697   1053

698   19. Hayati A., Mattsson M., Sandberg M., 2018. A wind tunnel study of wind-driven
699   airing through open doors. International Journal of Ventilation.
700   https://doi.org/10.1080/14733315.2018.1435027

701   20. Karava P., Stathopoulos T., Athienitis A.K., 2004. Wind driven flow through
702   openings – A review of discharge coefficients. International Journal of Ventilation
703   3:3, 255-266.

704   21. Karava P., Stathopoulos T., Athienitis A. K., 2007. Wind-induced natural
705   ventilation analysis. Solar Energy 81, 20-30.

706   22. Karava P., Stathopoulos T., Athienitis A.K., 2011. Airflow assessment in cross-
707   ventilated buildings with operable façade elements. Building and Environment 46,
708   266-279.

709   23. Kim Y.C., Yoshida A., Tamura Y., 2012. Characteristics of surface wind pressures
710   on low-rise building located among large group of surrounding buildings.
711   Engineering Structures 3, 18-28.

712   24. Kobayashi T., Sandberg M., Kotani H., Claesson L., 2010. Experimental
713   investigation and CFD analysis of cross-ventilated flow through single room
714   detached house model. Building and Environment 45, 2723-2734

715   25. Kobayashi T., Sandberg M., Fujita T., Lim E., Umemiya N., 2018. Simplified
716   estimation of wind-induced ventilation rate caused by turbulence for a room with
717   minute wind pressure difference. Proc. Roomvent &Ventilation 2018, Helsinki
718   (Finland).

719   26. Li B., Liu J., Gao J., 2015. Surface wind pressure tests on buildings with various
720   non-uniformity morphological parameters. Journal of Wind Engineering and
721   Industrial Aerodynamics 37, 14-24.

722   27. Li B., Wang L., Liu Y., Liu J., 2018. Drag distributions of non-uniform buildings
723   from surface pressure measurements in wind tunnel. Building and Environment 143,
724   618-631.

725   28. Oke T.R., 1988. Street design and urban canopy layer climate. Energy and Buildings
726   11, 103-113.

727   29. Sandberg M., Skote M., Westerberg U., Claesson L., Johansson A.V., 2004. Urban

728   morphology and windiness. Proc. COST Action C14, ISBN 2-93089-11-7, pp B.7.1-

729   B.7.10, Von Karman Institute, Rhode-Saint-Genèse (Belgium), May 5-7.

730   30. Santiago J.L., Martilli A., 2010. A dynamic urban canopy parameterization for

731   mesoscale models based on Computational Fluid Dynamics Reynolds-Averaged

732   Navier–Stokes microscale simulations. Boundary-Layer Meteorology 137, 417-439

733   31. Santiago J.L., Coceal O., Martilli A., 2013. How to parametrize urban-canopy drag

734   to reproduce wind-direction effects within the canopy. Boundary-Layer

735   Meteorology 149, 43-63.

736   32. Shetabivash H., 2015. Investigation of opening position and shape on the natural

737   cross ventilation. Energy and Buildings 93, 1-15.

738   33. Shirzadia M., Naghashzadegana M., Mirzaeib P.A., 2018. Improving the CFD

739   modelling of cross-ventilation in highly-packed urban Areas. Sustainable Cities and

740   Society 37, 451-465.

741   34. Tecle A., Bitsuamlak G.T., Jiru T.E., 2013. Wind-driven natural ventilation in a

742   low-rise building: a boundary layer wind tunnel study. Building and Environment

743   59, 275-289.

744   35. Tomas J.M., Eisma H.E., Pourquie M.J.B.M., Elsinga G.E., Jonker H.J.J.,

745   Westerweel J., 2017. Pollutant dispersion in boundary layers exposed to rural-to-

746   urban transitions: varying the spanwise length scale of the roughness. Boundary-

747   Layer Meteorology 163, 225-251.

748   36. VDI 3783 guidelines. Part 12 (2004) Environmental meteorology. Physical

749   modelling of flow and dispersion processes in the atmosphere boundary layer.

750   Application of wind tunnels. Düsseldorf (Germany).

751   37. VETEK. Datasheet 108AA (2014) Available at:

752   http://www.vetek.com/Dynamics/Documents/03d70901-8980-4b82-be3c-

753   aa112de353e0/Datasheet%20108AA%20Eng.pdf

754   38. Warren P.R., 1977. Ventilation through openings on one wall only. In C. J.

755   Hoogendorn & N.H. Afgar, eds. Energy conservation in heating, cooling and

756   ventilating buildings. Hemisphere, Washington DC, 189-209.

757   39. Zaki S.A., Hagishima A., Tanimoto J., Ikegaya N., 2011. Aerodynamic parameters
758   of urban building arrays with random geometries Boundary-layer Meteorology 138,
759   99-120.
760   40. Zu G., Lam K.M., 2018. Simultaneous measurements of wind velocity field and
761   wind forces on a square tall building. Advances in Structural Engineering.
762   https://doi.org/10.1177/1369433218770822